Editors' Suggestion

Electronic band structure of Sb_2Te_3

I. Mohelsky,[1] J. Wyzula,[1,2] F. Le Mardelé,[1] F. Abadizaman,[3] O. Caha,[3] A. Dubroka,[3] X. D. Sun,[1] C. W. Cho,[1] B. A. Piot,[1] M. F. Tanzim,[4] I. Aguilera,[4] G. Bauer,[5] G. Springholz,[5] and M. Orlita[1,6,*]

[1]*Laboratoire National des Champs Magnétiques Intenses, LNCMI-EMFL, CNRS UPR3228, Univ. Grenoble Alpes, Univ. Toulouse, Univ. Toulouse 3, INSA-T, Grenoble 38340, France*

[2]*Scientific Computing, Theory and Data Division, Paul Scherrer Institute, 5232 Villigen PSI, Switzerland*

[3]*Department of Condensed Matter Physics, Masaryk University, Kotlarská 2, 611 37 Brno, Czech Republic*

[4]*Institute for Theoretical Physics Amsterdam, University of Amsterdam, and European Theoretical Spectroscopy Facility (ETSF), 1090 GL Amsterdam, The Netherlands*

[5]*Institut für Halbleiter- und Festkörperphysik, Johannes Kepler Universität, Altenbergerstrasse 69, 4040 Linz, Austria*

[6]*Faculty of Mathematics and Physics, Charles University, Ke Karlovu 5, Prague 121 16, Czech Republic*

(Received 12 December 2023; accepted 15 March 2024; published 18 April 2024)

We report on Landau-level spectroscopy of an epitaxially grown thin film of the topological insulator Sb_2Te_3, complemented by ellipsometry and magnetotransport measurements. The observed response suggests that Sb_2Te_3 is a direct-gap semiconductor with the fundamental band gap located at the Γ point or along the trigonal axis, and its width reaches $E_g = (190 \pm 10)$ meV at low temperatures. Our data also indicate the presence of other low-energy extrema with a higher multiplicity in both the conduction and valence bands. The conclusions based on our experimental data are confronted with and to a great extent corroborated by the electronic band structure calculated using the *GW* method.

DOI: 10.1103/PhysRevB.109.165205

I. INTRODUCTION

The family of materials based on pnictogen and chalcogen atoms comprises a number of appealing topological systems [1,2]. Among others, it includes narrow-gap semiconductors Bi_2Se_3, Bi_2Te_3, and Sb_2Te_3, which were proposed [3] and confirmed as three-dimensional topological insulators at a very early stage of the topological epoch [4–6]. Nowadays, they belong to the best-known examples of systems with a nontrivial topology of the electronic band structure.

Lately, the emerged interest in topological aspects of matter, together with huge progress in the experimentation of surface-sensitive techniques angle-resolved emission spectroscopy (ARPES) and scanning tunneling microscopy/scanning tunneling spectroscopy, in particular, has caused our understanding of the bulk electronic band structure of these materials to often lag behind their intriguing surface states. Recent results of Landau-level (LL) spectroscopy measurements [7,8], combined with data from early magnetotransport experiments [9–11], clarified that Bi_2Se_3 and Bi_2Te_3 are both direct-gap semiconductors, the latter with a multiple-valley degeneracy ($N = 6$).

As compared to Bi_2Se_3 and Bi_2Te_3, the bulk band structure of Sb_2Te_3 remains, to a great extent, uncovered. The quantum oscillations experiments have so far been performed only on bulk *p*-type samples with rather high hole concentrations (above 10^{20} cm^{-3}). The interpretation suggested sixfold [12–16] or 12-fold [17] valley degeneracy, but also a more complex structure of the valence band, with sixfold and nondegenerated valleys combined [18]. While the single-valley degeneracy is connected with the center of the Brillouin zone (BZ) only, the sixfold degenerated band extrema may be located along the binary axes or in the mirror planes; see Fig. 1.

The band structure of Sb_2Te_3 has also been theoretically addressed several times [3,19–23]. The results of various *ab initio* approaches are not fully consistent, but at least indicate that the band extrema should be primarily located at the Γ point, along the $Z - \Gamma - Z$ line or in the mirror planes. Notably, the calculated energies of different conduction- or valence-band extrema often differ only by several tens of meV. This is likely beyond the precision of theoretical methods and calls for a detailed experimental inspection that may allow us to determine the location, width, and type of the fundamental band gap of Sb_2Te_3.

In this paper, we present a combined experimental and theoretical study of bulk electronic states in the Sb_2Te_3 topological insulator. Using magneto-optical, optical, and magnetotransport methods, we find that Sb_2Te_3 is a material with a direct-energy band gap. This gap reaches $E_g = (190 \pm 10)$ meV and is located in the center of the BZ or along the trigonal axis. Nevertheless, the valence and conduction bands also display other local extrema at low energies, most likely in the mirror planes, and therefore with a sixfold degeneracy.

II. SAMPLE PREPARATION, EXPERIMENTAL AND COMPUTATIONAL DETAILS

The studied Sb_2Te_3 epilayer with a nominal thickness of 300 nm (ellipsometry value 276 ± 2 nm) was grown

*milan.orlita@lncmi.cnrs.fr

Published by the American Physical Society under the terms of the Creative Commons Attribution 4.0 International license. Further distribution of this work must maintain attribution to the author(s) and the published article's title, journal citation, and DOI.

using molecular beam epitaxy on a 1-mm-thick (111)-oriented cleaved BaF_2 substrate. Compound Sb_2Te_3 and elemental Te sources were used for the control of the stoichiometry and composition. The deposition was carried out at a sample temperature of 290 °C at which a high-quality two-dimensional (2D) growth mode occurs as evidenced by reflection high-energy electron diffraction and atomic force microscopy. The grown Sb_2Te_3 layer has the trigonal axis oriented perpendicular to the substrate.

The prepared epilayer was characterized using x-ray diffraction measurements in the temperature range of $T =$ 77–300 K. At room temperature, the deduced lattice constants, $a = (0.4257 \pm 0.0002)$ nm and $c = (3.049 \pm 0.002)$ nm, compare well to the values reported in the literature [24]: $a = 0.4264$ nm and $c = 3.0458$ nm, respectively. This suggests that the epilayer is well relaxed. The experiments also show that when cooling down, a weak tensile stress (around 0.05%) appears as a result of different thermal contractions in BaF_2 and Sb_2Te_3.

To measure infrared magnetotransmission, radiation from a globar or a mercury lamp was analyzed by a commercial Bruker Vertex 80v Fourier-transform spectrometer. The radiation was then delivered via light-pipe optics to the sample kept in the helium exchange gas at the temperature $T = 2$ or 4.2 K and placed in a superconducting solenoid or in the resistive high-field magnet (below or above 16 T, respectively), both at the LNCMI in Grenoble.

Infrared radiation transmitted through the sample was detected by a composite bolometer, placed below the sample. The studied sample was probed in both Faraday and Voigt configurations, with the wave vector propagating along and perpendicular to the applied magnetic field, respectively. In the latter case, a linear polarizer was used to select the electric polarization oriented perpendicularly to the applied magnetic field. The measured transmission spectra T_B were normalized by the zero-field transmission T_0 and plotted in the form of relative magnetotransmission T_B/T_0 or, alternatively, as relative magneto-absorbance, $A_B = -\ln[T_B/T_0]$.

The optical response at $B = 0$ was deduced by the ellipsometry technique, with a commercial Woollam IR-VASE ellipsometer coupled to a closed He-cycle cryostat; for details, see Ref. [25]. Complementary magnetotransport measurements were realized using the standard lock-in technique on a sample with electrical contacts in the Hall-bar configuration, placed in the variable-temperature insert in a superconducting coil (up to 16 T).

The first-principles calculations were carried out with density functional theory (DFT) and the *GW* approximation, as implemented in the codes FLEUR [26] and SPEX [27] within the full potential linearized augmented plane waves (FLAPW) formalism. We used the same lattice parameters of Ref. [23]. The DFT calculations were performed using the generalized gradient approximation (GGA) of Perdew-Burke-Ernzerhof (PBE) [28] for the exchange-correlation functional. We used an angular momentum cutoff $l_{\max}$=10 and a plane-wave cutoff of 4.5 bohr^{-1}. The BZ was sampled using an $8 \times 8 \times 8$ k-point mesh, both in the DFT and the *GW* calculations.

A mixed product basis was used for the *GW* calculations, with an angular momentum cutoff of 5 and linear momentum cutoff of 2.9 bohr^{-1}. The number of bands was set to 500 for the calculation of the Green function and the polarization function. The spin-orbit-coupling (SOC) effect was incorporated with the method of Refs. [29,30], which ensured that the SOC effects were fully included in the Green function, the screened Coulomb potential, and the self-energy.

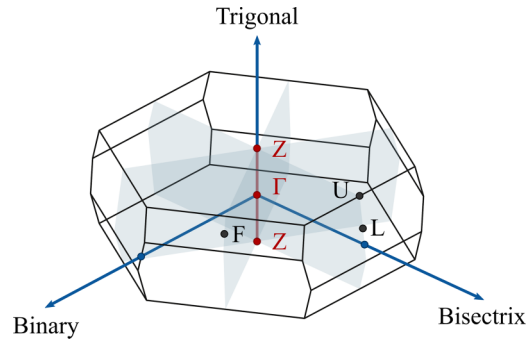

FIG. 1. Schematic view of the first BZ of Sb_2Te_3 with the mirror planes (gray planes) and trigonal, bisectrix, as well as binary axes indicated.

The k mesh used in the DFT and *GW* calculations ensures [23] that accurate maximally localized Wannier functions (MLWFs) [31] can be constructed. This was done with the help of the WANNIER90 library [32]. Using the Wannier-interpolation technique as discussed in Ref. [23], one can obtain (interpolated) energy eigenvalues (DFT or *GW*) in a denser mesh. We have used it to interpolate the *GW* eigenvalues in a $28 \times 28 \times 28$ mesh needed to converge the dielectric function. The latter was calculated from the random phase approximation (RPA) polarizability [27] taking the macroscopic average including local-field effects.

III. RESULTS AND DISCUSSION

A. Magneto-optics

The magneto-optical data collected on the explored Sb_2Te_3 epilayer at low temperatures in the midinfrared spectral range are presented in Figs. 2(a) and 2(b) as a stacked plot of relative magnetotransmission spectra T_B/T_0 and as a false-color plot of relative magneto-absorbance A_B, respectively. The data are dominated by two series of resonances—by the upper and lower set—that may be directly associated with excitations bringing electrons across the band gap, between Landau-quantized valence bands. In the following, we analyze this magneto-optical data and compare it with the results of complementary techniques, in order to associate the two sets with particular locations in the BZ. In our magneto-optical data, we did not identify any contribution directly attributable to surface states [6,33–35].

Let us now analyze the observed transitions in terms of their position, B dependence, and intensity in greater detail. The transitions in both series follow a weakly sublinear-in-B dependence and extrapolate to a finite photon energy in the limit of a vanishing magnetic field. Such behavior is typical of narrow-gap semiconductors and can be, in this particular case, well reproduced using a simple two-band Hamiltonian often referred to as the model of massive Dirac electrons. In this simple model, with only two material parameters, the

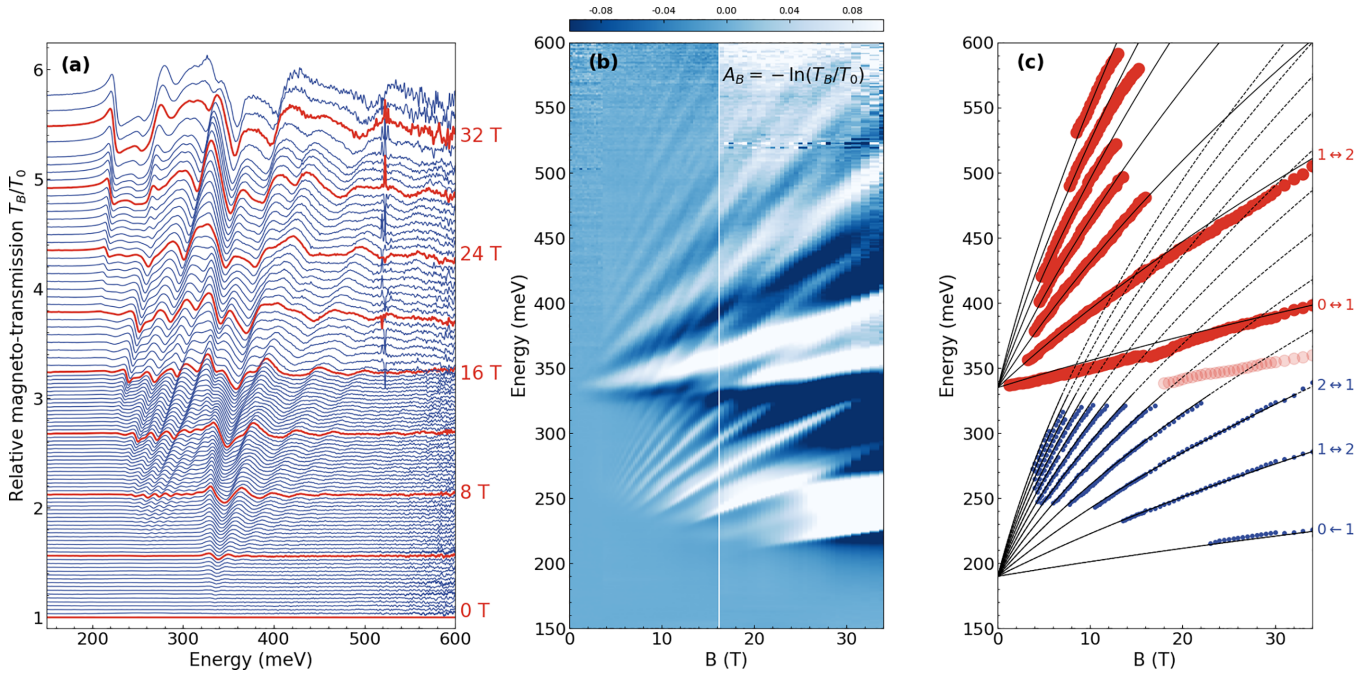

FIG. 2. Magneto-optical response of Sb_2Te_3 in the midinfrared spectral range at $T = 4.2$ K. (a) Relative magnetotransmission spectra T_B/T_0, plotted at selected values of the applied magnetic field B. (b) A false-color plot of relative magneto-absorbance $A_B = -\ln[T_B/T_0]$. (c) Extracted positions of interband inter-LL resonances in the lower (blue) and upper (red) series. The light-red color is used for the satellite line discussed in the main text. The solid and dashed lines are fits using a simple two-band (massive Dirac-type) model; see the main text for a description.

conduction (+) and valence (−) bands display hyperbolic profiles: $E = \pm\sqrt{\Delta^2 + \hbar^2 v^2 k^2}$, where v is the velocity parameter and 2Δ represents the width of the band gap. The strong enough magnetic field transforms these bands in dispersive one-dimensional Landau bands, with the band edge energies of $E_n = \pm\sqrt{\Delta^2 + 2v^2\hbar n|eB|}$, for $n \geqslant 0$.

Taking the corresponding selection rules for electric-dipole excitations for massive Dirac electrons [7,36,37], i.e., $n \to n \pm 1$, the model reproduces the experimentally determined positions of interband inter-LL excitations very well; see Fig. 2(c). For the lower set, the parameters read $2\Delta_L = (190 \pm 10)$ meV and $v_L = (4.1 \pm 0.2) \times 10^5$ m/s. For the upper set, we obtained $2\Delta_U = (340 \pm 10)$ meV and $v_U = (7.5 \pm 0.5) \times 10^5$ m/s. The extracted parameters allow us to get estimates of the band-edge masses, $m_L = \Delta_L/v_L^2 = (0.10 \pm 0.01)m_0$ and $m_U = \Delta_U/v_U^2 = (0.055 \pm 0.005)m_0$, assuming that the electron-hole symmetry is preserved. Here, m_0 stands for the bare electron mass.

Let us note that the successful application of the simplified, massive Dirac model is, to a certain extent, surprising. Clearly, we deal with a topological insulator, and the lower series of inter-LL excitation is—as justified *a posteriori* in the paper—associated with the center of the BZ where the band structure is clearly inverted. In such a case, it is common to expand the Hamiltonian to include a diagonal dispersive term Mk^2 which effectively describes the extension of the band inversion in the reciprocal space; see, e.g., Refs. [36–39]. This term impacts the LL spectrum mainly at high energies, i.e., well above the band gap. There, the LLs gain a linear-in-B dependence (see Ref. [7]) that contrasts with the $\sqrt{B}$ dependence typical of Dirac electrons (with $M \equiv 0$). In the case of Sb_2Te_3, we were only able to set the upper limit for the inversion parameter: $|M| < 10\,\text{eV}^2$. For higher values, the theoretical B dependence of inter-LL excitations starts to visibly deviate from the experimental data. Another deviation from the simple massive Dirac model appears for the upper set in high magnetic fields. A satellite transition emerges at $B > 15$ T below the $0 \leftrightarrow 1$ line, which disperses approximately with the same slope [light-red full circles in Fig. 2(c)]. This additional line may correspond to an excitation from/to a shallow impurity state.

Other relevant pieces of information can be extracted from the intensity of the observed inter-LL excitations. Individual inter-LL transitions in the lower set emerge with increasing B one by one, thus indicating a pronounced occupation effect. The quantum limit, with the Fermi energy in the lowest LL, is only achieved above 20 T when the transition $0 \leftrightarrow 1$ appears in the response [$\hbar\omega \approx 200$ meV; see Fig. 2(b)]. In fact, this is a well-known Moss-Burstein shift [40,41], but with the onset of interband absorption driven by the B-dependent Fermi energy. This implies that the lower set of transitions comes from a particular location in the BZ with a non-negligible density of free charge carriers. In contrast, no occupation effect is visibly manifested in the upper set. This indicates a lower, or even negligible carrier density in the concerned bands.

Magneto-optical experiments at lower photon energies, below the reststrahlenband of the BaF_2 substrate, were performed as well; see Fig. 3. As expected, the transmission of the sample is low due to absorption on free charge carriers (Drude-type absorption). This takes a form of cyclotron resonance (CR) absorption when the magnetic field is applied.

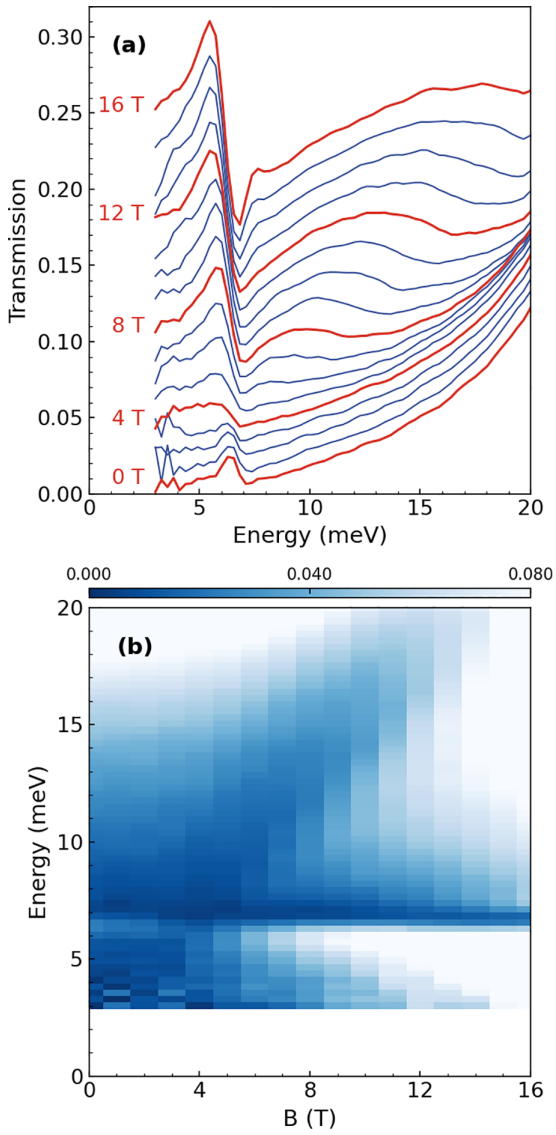

FIG. 3. Magneto-optical response of Sb_2Te_3 in the far-infrared spectral range at $T = 4.2$ K. (a) Magnetotransmission spectra T_B, normalized by the transmission of a bare BaF_2 substrate, are plotted for selected values of B. The same data in the form of a false-color plot are presented in (b). In both panels, pronounced coupling of the CR mode with the phonon mode at 7 meV is observed (E_u mode [42]).

Unfortunately, the precise readout of the CR energy and the extraction of the effective mass is not straightforward due to strong coupling, primarily due to a dielectric effect, between a pronounced phonon mode ($E_u \approx 7$ meV; see Ref. [42]) and free charge carriers. Nevertheless, a rough estimate of the effective mass $m_c \approx 0.08 m_0$ from the B-dependent minimum in the transmission response approaches the Dirac mass m_L deduced for the lower set of interband excitations.

To probe the anisotropy of the magneto-optical response, a complementary magneto-optical experiment was carried out with B oriented perpendicular to the trigonal axis of Sb_2Te_3 ($B \perp c$). In the case of a thin layer, such an experiment is only possible in the Voigt configuration. To follow transitions active within the same set of selection rules as in the Faraday configuration, we used a linear polarizer and selected radiation with the electric field component perpendicular to the magnetic field ($B \perp E$). The data collected in the Faraday and Voigt configuration are compared in Fig. 4.

Interestingly, the lower set of inter-LL excitations vanishes completely in the Voigt configuration ($B \perp c$). This suggests a pronounced anisotropy of the band structure at the related location in the BZ, with the bands too flat along the c direction to enter the Landau-quantized regime at applied magnetic fields. In contrast, the upper series of transitions shows nearly isotropic behavior. Again, the observed response (i.e., the upper set) can be well reproduced using the model of massive Dirac electrons, with an identical band gap $2\Delta_U$, but with the velocity parameter slightly lowered, $v_U = (6.0 \pm 0.5)$ m/s. Let us note that two independent experiments were realized in the Voigt configuration, with the sample rotated by 90 degrees around the trigonal axis to probe the in-plane anisotropy. These measurements provide us with nearly identical results, consistent with a fairly low in-plane anisotropy (weak trigonal warping).

To sum up, the magneto-optical response of Sb_2Te_3 at low photon energies is surprisingly complex. It is dominated by two or, when the expected multiplicity of the band extrema is considered, more-than-two distinct locations in the BZ. These differ considerably in the extracted band gap, by the characteristic anisotropy of the local band structure, but also by the density of free charge carriers at the local band extrema. The observed magneto-optical response suggests that Sb_2Te_3 is a direct-gap semiconductor with the band gap reaching $E_g = (190 \pm 10)$ meV.

B. Magnetotransport

To complement our magneto-optical experiments, we performed a series of magnetotransport measurements on the same sample. Both transversal and longitudinal components of the magnetoresistivity tensor—with B applied along the trigonal axis of Sb_2Te_3—were recorded, with the latter also as a function of temperature; see Fig. 5(a). The Hall signal was linear in the applied magnetic field and the sign indicated p-type conductivity typical of Sb_2Te_3 [12–16]. The slope corresponds to the total hole density of $p_H = (1.4 \pm 0.1) \times 10^{19}$ cm^{-3}. The presence of this non-negligible hole concentration in single-crystalline bulk or epitaxial layers of Sb_2Te_3 may be caused by the rather similar cation and anion electronegativities [43] in this compound. During crystal growth, this leads to a large number of negatively charged antisite defects, which result from the occupation of some Te sites in the Sb_2Te_3 lattice by Sb and which produce one hole for one antisite defect [43–45], and furthermore also leads to the formation of Sb vacancies [45].

The longitudinal component of magnetoresistance exhibited well-visible Shubnikov–de Haas oscillations. Our analysis based on the fast Fourier transformation indicated two oscillation periods having frequencies of $F_1 = (45 \pm 5)$ T and $F_2 = (15 \pm 5)$ T; see Fig. 5(b). This indicates the existence of two types of hole Fermi surfaces in our sample. Below, we refer to them as larger and smaller ones, respectively. Interestingly, no signs of splitting due to spin were observed. This may be surprising in a material with a particularly strong spin-orbit interaction. Nevertheless, in the

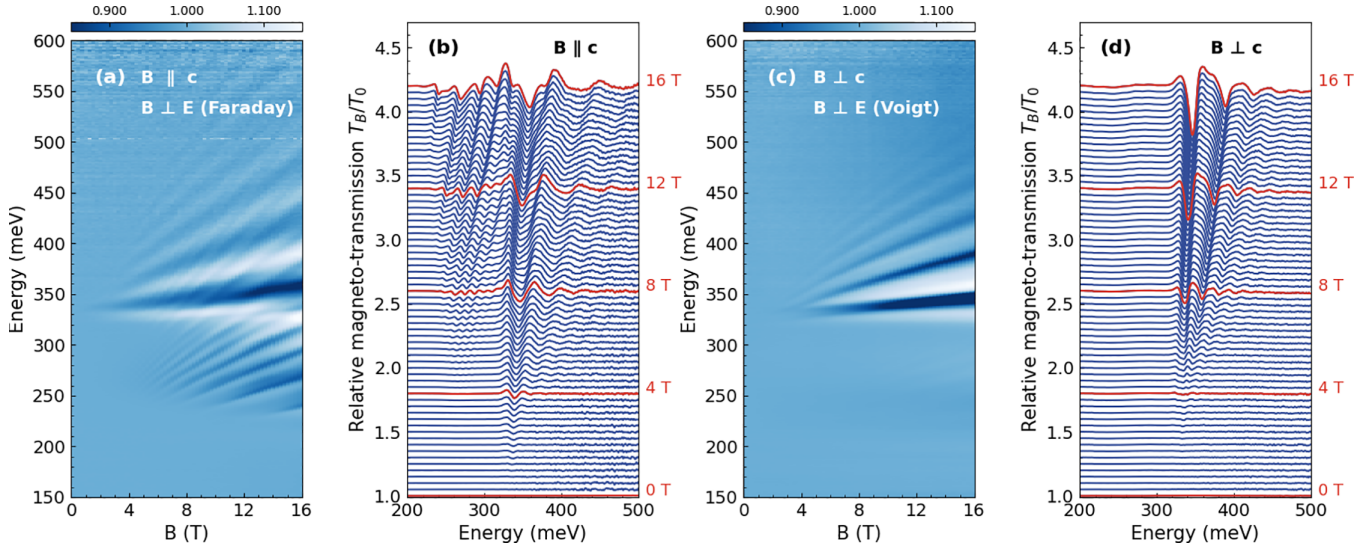

FIG. 4. Magneto-optical response of Sb_2Te_3 in the midinfrared spectral range at $T = 4.2$ K in the Faraday and Voigt (both $B \perp E$) configurations. Relative magnetotransmission spectra T_B/T_0, collected in the Faraday and Voigt configurations, are plotted in a form of (a), (c) false-color plots and (b), (d) stacked plots, respectively.

sister material Bi_2Se_3, the same effect is present as well and explained as due to spin splitting that matches multiples of the cyclotron energy [46]. The Lifshitz-Kosevitch-like analysis of the oscillations' damping with temperature was only possible for the dominant oscillations, corresponding to the larger Fermi surface. It provided us with the effective mass of $m_1 = (0.11 \pm 0.02)m_0$. When the approximation of a strictly parabolic band is used, this gives us an estimate of the Fermi energy around 40–50 meV.

To explore the anisotropy of the Fermi surfaces, we have also traced the Shubnikov–de Haas oscillations as a function of the angle θ between the trigonal axis and the direction of the applied magnetic field ($\theta = 0$ equivalent to $B \| c$). In our experiment, the magnetic field was oriented randomly with respect to the in-plane (a-b) crystallographic axes. The result of the frequency analysis is plotted in the form of a false-color plot in Fig. 5(c).

Interestingly, the angle dependence is distinctively different for the two identified oscillation periods. The frequency F_1, belonging to the larger Fermi surface, increases monotonically with the angle and reaches roughly 4× its original value at $\theta = 90$ degrees. This excludes the possibility that we observe the response of electrons in the surface states, recently reported on even thinner Sb_2Te_3 layers [47]. The amplitude

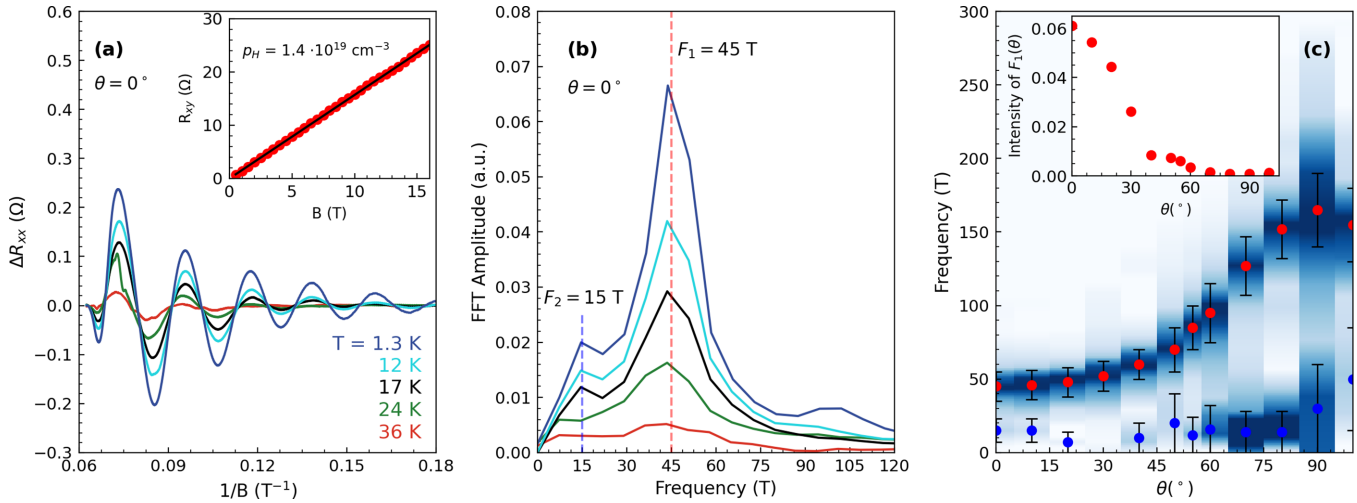

FIG. 5. Magneto-transport experiments. (a) Temperature dependence of background-removed Shubnikov–de Haas oscillations in Sb_2Te_3 with B applied along the trigonal axis. Inset: The corresponding Hall resistance at $T = 1.36$ K, showing linear-in-B dependence. (b) Frequency spectra of $1/B$-periodic Shubnikov–de Haas oscillations at selected temperatures. (c) False-color plot: frequency spectra of $1/B$-periodic Shubnikov–de Haas oscillations as a function of the angle θ between the trigonal axis and magnetic field. To visualize the angle dependence, individual experimental traces were normalized by their maximum. Inset: The angle dependence of the oscillations' amplitude.

of oscillations drops significantly [see the inset of Fig. 5(c)], becoming very weak at angles around $\theta = 90$ degrees. The larger Fermi surface is thus greatly elongated in the direction of the trigonal axis. The frequency F_2—corresponding to the smaller Fermi surface—remains constant as a function of θ within the experimental accuracy, and hence this Fermi surface is approximately spherical.

Let us note that a different angle dependence was observed in early magnetotransport studies of Sb_2Te_3. The observed oscillation period did not evolve monotonically with θ [12] and even signs of splitting appeared when B was not parallel with the trigonal axis [17]. Such behavior was interpreted as due to the multiple-valley structure of the topmost valence band (with the valley degeneracy $N = 6$ or 12). It is important to stress, however, that those studies were performed on crystals with almost an order-of-magnitude-larger hole density (around 10^{20} cm^{-3}).

Having quantified the anisotropy of the larger Fermi surface, we may estimate the related per-valley density of holes. Let us assume that the band, even though profoundly anisotropic, still has a strictly parabolic profile at the concerned energies. The observed angle dependence of F_1 implies a relatively large difference—by a factor of 16—between the effective masses perpendicular to and along the trigonal axis: $m_1^{\perp} = (0.11 \pm 0.02)m_0$ and $m_1^{\parallel} = (1.8 \pm 0.3)m_0$, respectively. This allows us to estimate, taking the frequency $F_1 = 45$ T at $\theta = 0$, the corresponding hole density per valley: $p_1 = (m_1^{\parallel}/m_1^{\perp})^{1/2}(2eF_1/\hbar)^{3/2}/(3\pi^2) = 7 \times 10^{18}$ cm^{-3}.

The extracted per-valley hole density p_1 represents one-half of the total hole density p_H estimated in the Hall experiments. Even though there exists some uncertainty in the Hall readout of the carrier density in systems with two types of charge carriers, this suggests that the larger hole pocket might be located at the Γ point ($N = 1$). Alternatively, the double valley degeneracy, $N = 2$, with two larger hole pockets located along the trigonal axis (along the $Z - \Gamma - Z$ line), is also possible. A higher valley degeneracy, $N = 6$ or even $N = 12$, is not consistent with our findings since $Np_1 \gg p_H$. Independently of the number of valleys that is concluded, each one is always considered to be twice degenerate due to spin.

The extracted properties of the larger hole pocket, i.e., the anisotropy, effective mass, and Fermi energy, remarkably resemble the analogous parameters deduced for the lower set of interband inter-LL transitions in Fig. 2. Hence, it is plausible to assume that they have their origin in the very same location of the BZ. This implies that the fundamental direct band gap of Sb_2Te_3 is located at the Γ point ($N = 1$) or, alternatively, along the $Z - \Gamma - Z$ line ($N = 2$); cf. Fig. 1.

Assigning the larger Fermi surface, observed in magnetotransport experiments, to the center of the BZ, one may speculate about the location(s) of the smaller one(s). It is plausible to assume that they may be positioned away from the trigonal axis—on the binary axis, in the mirror place (both $N = 6$), or in a general location lacking any higher symmetry ($N = 12$). Most likely, those were the hole pockets which dominated the response in early quantum oscillation experiments performed on bulk samples with a significantly higher hole density [12,17].

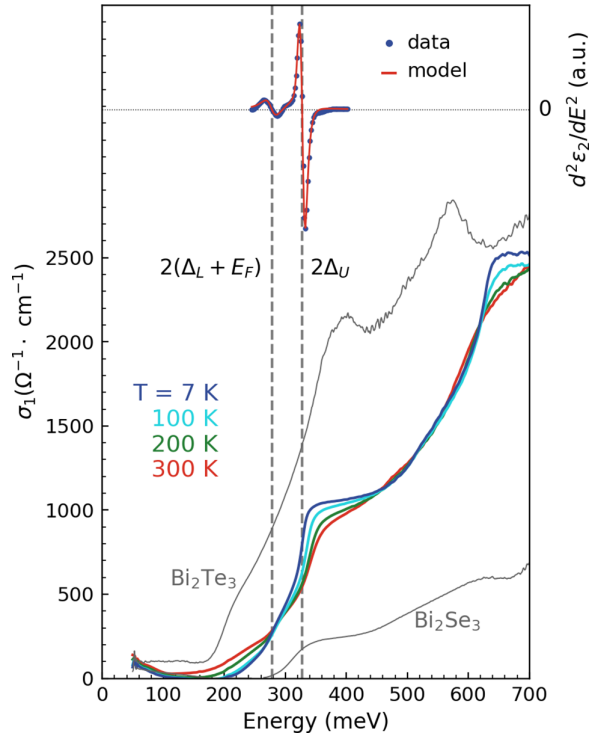

FIG. 6. Real part of optical conductivity of Sb_2Te_3 deduced using ellipsometry at $T = 7, 100, 200$ and 300 K. The vertical dashed lines mark the position of two inflection points (at $T = 7$ K) in the imaginary part of the dielectric function, found as zero points of the second derivative; see the upper part. They are associated with two onsets of interband absorption in the data. The gray curves for Bi_2Se_3 and Bi_2Te_3 are replotted from Refs. [25] and [8], respectively.

C. Ellipsometry measurements

Let us now confront our conclusions so far with the result of the ellipsometry experiments. These were performed at $B = 0$ and at varying T: from room temperature down to 7 K. The deduced real part of optical conductivity, i.e., the optical constant most relevant for this work, is plotted in Fig. 6. It has a double-step onset at low photon energies, which smears out with the increasing temperature. To estimate the positions of these two onsets, we used the critical point model [48] and searched for zero points in the second derivative of the imaginary part of the dielectric function (plotted in the top part of Fig. 6). The positions of onsets are marked by two vertical dashed lines at 277 and 329 meV in Fig. 6.

The lower inflection point matches well with the expected onset of interband absorption at the Γ point (or along the trigonal axis), corresponding to the fundamental band gap enhanced by twice the Fermi energy at the larger hole pocket: $2(\Delta_L + E_F)$. This is due to the above-mentioned Moss-Burstein shift [40,41] that is typical of degenerate semiconductors with a low electron-hole asymmetry. The upper inflection point corresponds well to the onset of interband absorption at the energy of the local band gap $2\Delta_U$. It is worth noting that apart from smearing that is clearly visible in the spectra, the basic character of the zero-field

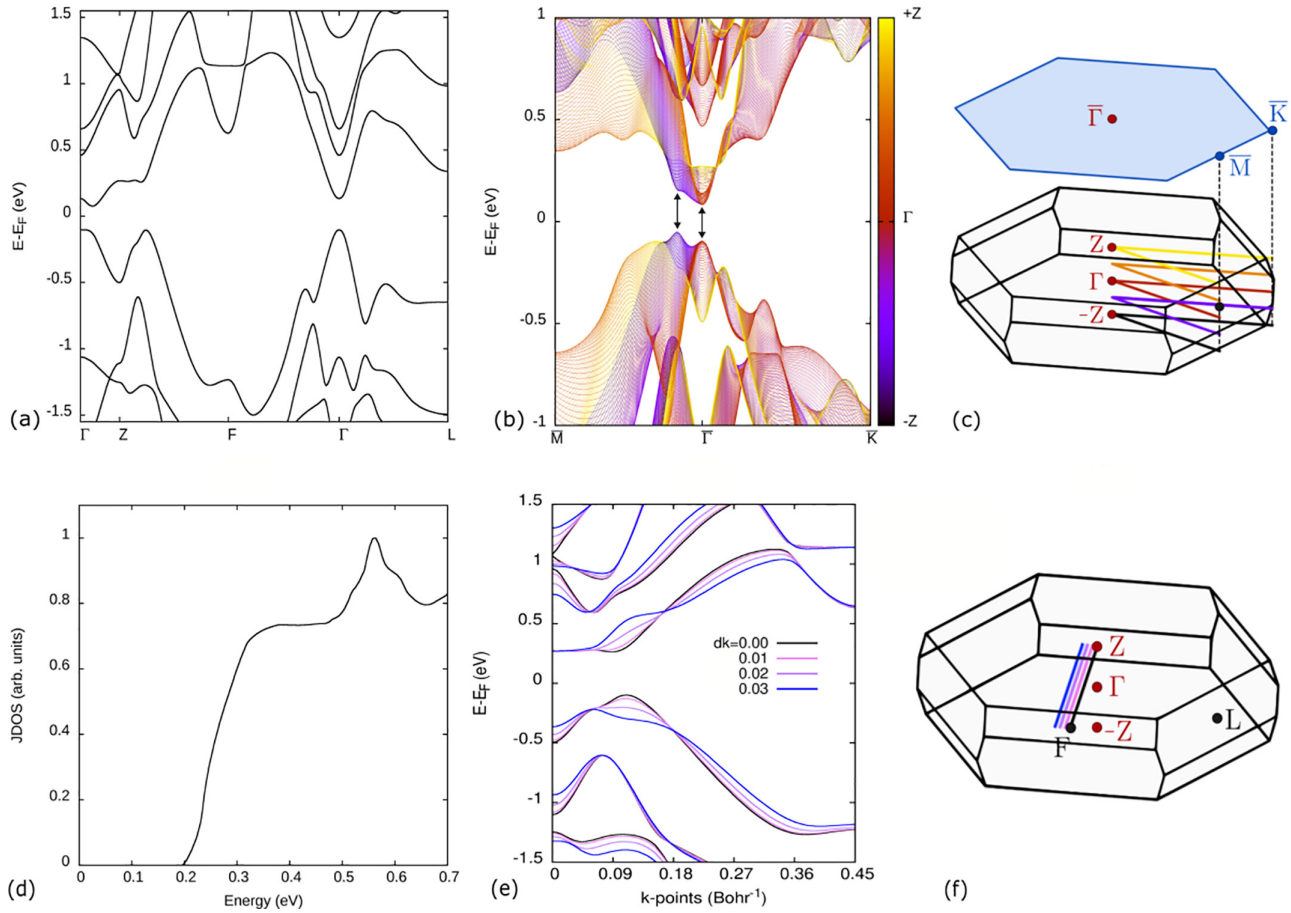

FIG. 7. Band structure of Sb_2Te_3 calculated using the *GW* method along different paths of the BZ. (a) Standard high-symmetry path of the bulk BZ. (b) Bulk bands projected on the surface (2D) BZ. Each line corresponds to a path in the bulk BZ that projects onto the path $\bar{\mathrm{M}} - \bar{\Gamma} - \bar{\mathrm{K}}$ in the surface BZ. The color of the bands represents the k_z component of the path. The paths and the corresponding colors are indicated in (c). (d) The calculated joint density of states at low photon energies. (e) Bands along the Z − F path of the bulk (blue) and three paths slightly shifted with a fixed k_z. This shows that the maximum and minimum are indeed located along the Z − F line and therefore have sixfold degeneracy ($N = 6$). The paths and colors corresponding to (e) are shown in (f).

optical response does not change with an increasing temperature. This implies that the band structure is robust against small temperature-induced strain/stress observed in the x-ray diffraction experiments.

It is instructive to compare the zero-field optical response of Sb_2Te_3 with sibling materials, i.e., Bi_2Se_3 and Bi_2Te_3, in which the valley degeneracy of the fundamental band gap is consensually established: $N = 1$ and $N = 6$, respectively. Interestingly, the profile of interband absorption in Bi_2Se_3 resembles—by its shape and amplitude—the first step in the absorption of Sb_2Te_3, just shifted towards higher energies. On the other hand, at higher photon energies, the optical conductivity of Bi_2Te_3 has the profile and overall strength similar to Sb_2Te_3, only shifted towards lower energies.

The above considerations are qualitative only, but they are in line with the above concluded single- or, at most, double-valley degeneracy of the fundamental direct band gap of $2\Delta_L = 190$ meV in Sb_2Te_3. In addition, they point towards the sixfold valley degeneracy of the upper (local) band gap of $2\Delta_U = 340$ meV. We suggest that this local band gap can be associated with the smaller hole pocket (the frequency F_2) observed in magnetotransport experiments.

D. Comparison with output of *GW* calculations

Let us now compare our inferences—made, so far, solely via the analysis of the collected experimental data—with the electronic band structure calculated using the *GW* approach. The band structure obtained theoretically along the selected directions of the BZ is plotted in Fig. 7(a). A series of band structure cuts is also depicted in Fig. 7(b). These were made for selected values of k_z along particular directions in the reciprocal space [see Fig. 7(c)] and, finally, projected to the surface (2D) BZ.

In the big picture, the calculated band structure is in very good agreement with our conclusions based solely on the experimental data. The extrema of electronic bands relevant for low-energy excitations targeted in our experiments are indeed located at the Γ point, along the $Z - \Gamma - Z$ line, and in the mirror planes. The calculations suggest the existence of two nearly degenerate maxima of the topmost valence band. This is consistent with the appearance of two series of interband inter-LL transitions in the magneto-optical response (Fig. 2), as well as two onsets in the zero-field optical conductivity (Fig. 6). The vertical double arrows in Fig. 7(b) indicate the

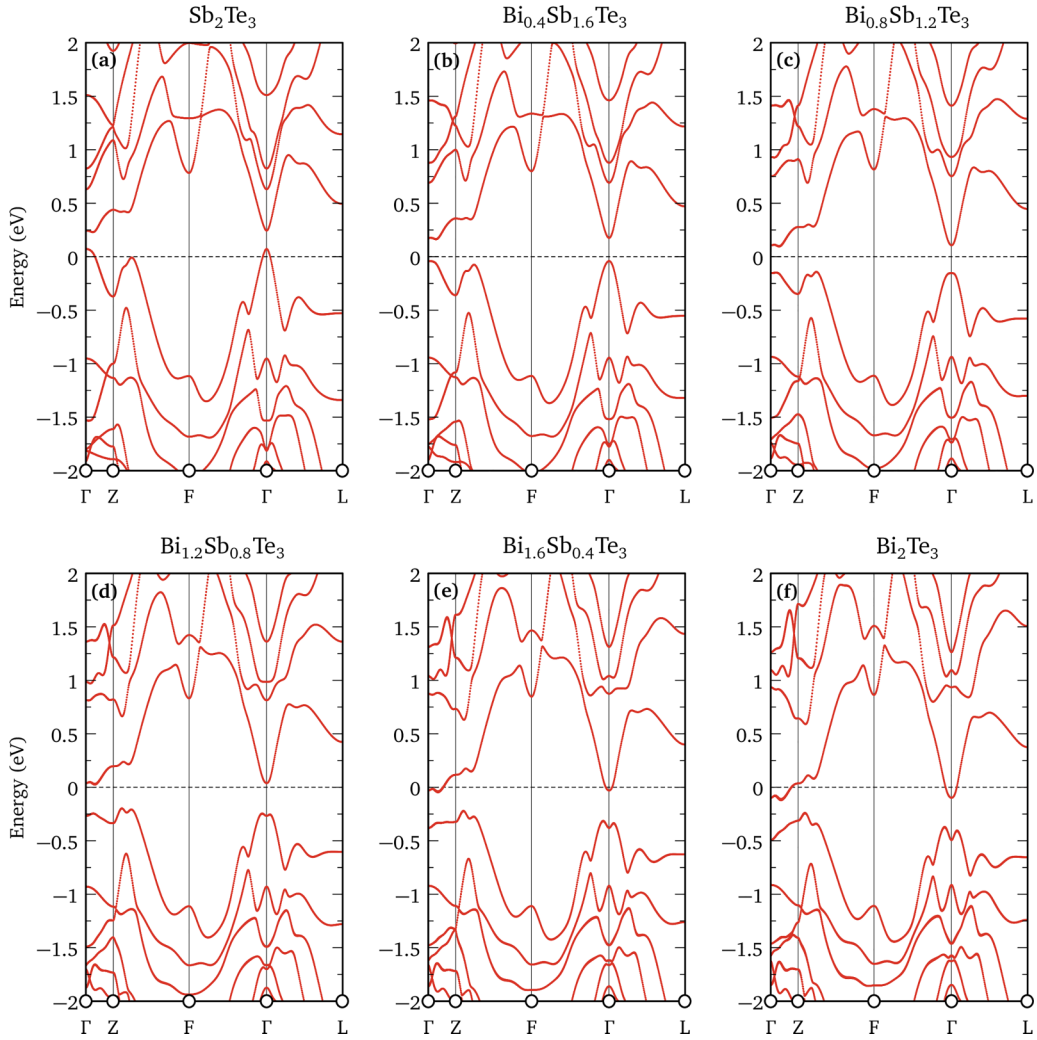

FIG. 8. The electronic band structure of $(Sb_{1-x}Bi_x)_2Te_3$ calculated using the *GW* tight-binding method [23] along selected directions for the bismuth content: $x = 0$, 0.2, 0.4, 0.6, 0.8, and 1.

corresponding locations in the BZ. The predicted band gap is slightly below 200 meV, a value perfectly in line with our optical and magneto-optical data ($2\Delta_L$). The calculations also suggest fairly large anisotropy (in the direction along versus perpendicular to the trigonal axis) of the global valence-band maximum at the Γ point. In addition, the calculated steplike nature of the joint density of states [Fig. 7(d)] compares rather well with the onset of interband absorption visualized by ellipsometry experiments (Fig. 6).

Having said this, let us compare the experimental findings with theoretical predictions in greater detail to identify the existing differences. While our transport experiments on the *p*-type sample conclude, at most, a double degeneracy of the global valence-band maximum, a sixfold degeneracy is suggested by the calculations [Fig. 7(b)]. This discrepancy is also related to another difference: The calculations imply an indirect type of band gap, while the experimental data are rather consistent with a direct one. Both discrepancies have the same origin: the theoretical prediction of the two maxima in the valence band with similar energies. The highest one [the absolute valence-band maximum (VBM)] lies on the mirror plane (degeneracy $N = 6$). To confirm this, Figs. 7(e) and 7(f) show the band structure for three other off-symmetry lines in the BZ parallel to the $Z - F$ line (i.e., parallel to the mirror plane). All paths have the same k_z component and deviate from each other by 0.01 Bohr^{-1} in-plane. The bands show that the VBM indeed lies along the $Z - F$ line and is thus sixfold degenerate ($N = 6$). The second one, approximately 40 meV below, is at the Γ point (degeneracy $N = 1$). However, as we discussed in Ref. [22], the relative energy between these two maxima is extremely sensitive to the details of the calculations. For example, a different set of lattice parameters used in the calculation can shift the valence-band maximum from one position to the other (see Fig. 2 of Ref. [22]). Therefore, in this case, the band structure calculations cannot give a definitive answer about which of the two is the absolute maximum.

It is interesting to compare these findings to the band structure of the sister compound Bi_2Te_3. There, a consensus exists in the literature, both in experimental studies [8,10] and in theoretical calculations, that the valence band is characterized by six pronounced global maxima located in the mirror planes ($N = 6$). The results of the *GW* calculations performed for the mixed compound $(Sb_{1-x}Bi_x)_2Te_3$ show such a trend when the Sb-to-Bi ratio increases. This is shown in

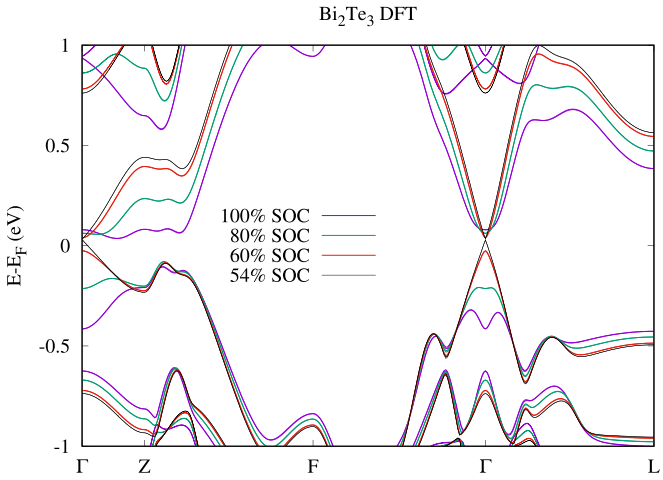

FIG. 9. DFT calculations in the generalized gradient approximation (GGA) of Bi_2Te_3 performed with the FLAPW code FLEUR [26]. The SOC strength is reduced from 100% to 54%. After that, the system undergoes a topological phase transition and becomes trivial.

Fig. 8 in the Appendix, where we also discuss the role of the spin-orbit interaction in this crossover (Fig. 9). Namely, the gradual increase in the bismuth concentration suppresses the valence-band maximum at the Γ point and enhances the maxima in the mirror planes (Z-F direction). These latter maxima become the global ones for $x > 0.6$. This picture is also consistent with conclusions of early quantum-oscillation experiments performed on the mixed $(Sb_{1-x}Bi_x)_2Te_3$ crystals [13]. The comparison of band structure parameters deduced in this work for Sb_2Te_3 with those for Bi_2Te_3 [8] is made in Table I .

Finally, we have experimentally shown that besides the fundamental band gap in the center of the BZ, the band structure also comprises additional, local energy band gaps, located most likely in the mirror planes and with fairly high, in their vicinity, isotropic bands. However, these additional band gaps are not clearly identified in our calculations. Even though such a maximum of the calculated topmost valence band can be found in the mirror plane, the shape of the rather shallow counterpart in the conduction band would not allow one to form a well-defined Landau quantization at the scale seen in our experimental data.

IV. CONCLUSIONS

We conclude that antimony telluride is a semiconductor with a direct energy band gap of $E_g = (190 \pm 10)$ meV at low temperatures, which is located at the center of the BZ or, alternatively, along the trigonal axis. In the observed response, we also do identify additional local maxima of the valence band, nearly degenerate with the global one, which form additional (local) direct gaps with the width of (340 ± 10) meV and display the sixfold valley degeneracy (mirror planes). Our findings are in fairly good agreement with the electronic band structure calculated using the *GW* method, thus demonstrating the high predictive power of this advanced theoretical technique.

ACKNOWLEDGMENTS

The authors acknowledge the support of the LNCMI-CNRS in Grenoble, a member of the European Magnetic Field Laboratory (EMFL). The work has been supported by the ANR projects DIRAC3D (Grant No. ANR-17-CE30-0023) and COLECTOR (Grant No. ANR-19-CE30-0032). This research was supported by the NCCR MARVEL, a National Centre of Competence in Research, funded by the Swiss National Science Foundation (Grant No. 205602). I.A. and M.F.T. acknowledge the computing time granted through SURF on the Dutch National Supercomputer Snellius. X.D.S. and B.A.P. acknowledge support from ANR Grant No. ANR-20-CE30-0015-01. We acknowledge the support by the project Quantum materials for applications in sustainable technologies, Grant No. CZ.02.01.01/00/22_008/0004572, the Czech Science Foundation (GACR) under Project No. GA20-10377S, and the CzechNanoLab Research Infrastructure supported by MEYS CR (Grant No. LM2023051). For the first-principles calculations, the computational resources were provided by the Dutch national e-infrastructure with the support of the SURF Cooperative under Grant No. EINF-5380.

APPENDIX: ELECTRONIC BAND STRUCTURE OF $(Sb_{1-x}Bi_x)_2Te_3$

Following the approach described in Ref. [23], we can use the *GW* calculations to construct tight-binding Hamiltonians for the parent compounds Sb_2Te_3 and Bi_2Te_3, which will allow us to simulate alloys with intermediate Sb and Bi concentrations. These tight-binding Hamiltonians are expressed in a basis of Wannier functions and there are no adjustable parameters: the Hamiltonian matrix elements are fully determined by the *GW* calculation of these two compounds. We used a $6 \times 6 \times 6$ k-point mesh for these calculations. A doping was simulated for the parent compounds by fitting the calculated band extrema to the ARPES results from [49]. To simulate the band structures of the alloys in Fig. 8, the

TABLE I. Summary of band structure parameters deduced for Sb_2Te_3 in this work compared to those of Bi_2Te_3 taken from Ref. [8]. The reported band-edge mass corresponds to both electrons and holes, thus completely neglecting a possible electron-hole asymmetry.

Material	Direct band gap (meV)	Location in Brillouin zone	Valley degeneracy	Effective band-edge mass (m_0)
Sb_2Te_3	190 ± 10	Γ (or $Z - \Gamma - Z$)	1 (or 2)	$a - b$ plane: 0.11 ± 0.02 c axis: 1.8 ± 0.3
	340 ± 10	Mirror planes	6	0.055 ± 0.005
Bi_2Te_3 [8]	175 ± 10	Mirror planes	6	0.070 ± 0.005

tight-binding parameters are smoothly varied between those of the parent compounds using the virtual crystal approximation (VCA).

It is worthwhile to note that the qualitative change of the $(Sb_{1-x}Bi_x)_2Te_3$ band structure, from one to six maxima in the valence band, when Sb is gradually replaced by Bi, can be explained in terms of the increasing strength of the spin-orbit interaction that is significantly stronger for the latter element. To elucidate this, we present, in Fig. 9, the DFT calculations of Bi_2Te_3 in which we artificially reduced the spin-orbit strength from 100% down to 54%, corresponding to the point of a topological phase transition. For lower spin-orbit interaction strengths, the system becomes topologically trivial. The results of this analysis are shown in Fig. 9 and suggest that the existence of the two competing valence-band maxima in Sb_2Te_3 is indeed a consequence of the lower SOC strength in Sb_2Te_3 with respect to Bi_2Te_3.

[1] M. Z. Hasan and C. L. Kane, *Colloquium:* Topological insulators, Rev. Mod. Phys. **82**, 3045 (2010).

[2] X.-L. Qi and S.-C. Zhang, Topological insulators and superconductors, Rev. Mod. Phys. **83**, 1057 (2011).

[3] H. Zhang, C.-X. Liu, X.-L. Qi, X. Dai, Z. Fang, and S.-C. Zhang, Topological insulators in Bi_2Se_3, Bi_2Te_3 and Sb_2Te_3 with a single Dirac cone on the surface, Nat. Phys. **5**, 438 (2009).

[4] D. Hsieh, Y. Xia, D. Qian, L. Wray, J. Dil, F. Meier, J. Osterwalder, L. Patthey, J. Checkelsky, N. P. Ong *et al.*, A tunable topological insulator in the spin helical Dirac transport regime, Nature (London) **460**, 1101 (2009).

[5] Y. L. Chen, J. G. Analytis, J.-H. Chu, Z. K. Liu, S.-K. Mo, X. L. Qi, H. J. Zhang, D. H. Lu, X. Dai, Z. Fang, S. C. Zhang, I. R. Fisher, Z. Hussain, and Z.-X. Shen, Experimental realization of a three-dimensional topological insulator, Bi_2Te_3, Science **325**, 178 (2009).

[6] D. Hsieh, Y. Xia, D. Qian, L. Wray, F. Meier, J. H. Dil, J. Osterwalder, L. Patthey, A. V. Fedorov, H. Lin, A. Bansil, D. Grauer, Y. S. Hor, R. J. Cava, and M. Z. Hasan, Observation of time-reversal-protected single-Dirac-cone topological-insulator states in Bi_2Te_3 and Sb_2Te_3, Phys. Rev. Lett. **103**, 146401 (2009).

[7] M. Orlita, B. A. Piot, G. Martinez, N. K. S. Kumar, C. Faugeras, M. Potemski, C. Michel, E. M. Hankiewicz, T. Brauner, C. Drašar, S. Schreyeck, S. Grauer, K. Brunner, C. Gould, C. Brüne, and L. W. Molenkamp, Magneto-optics of massive Dirac fermions in bulk Bi_2Se_3, Phys. Rev. Lett. **114**, 186401 (2015).

[8] I. Mohelský, A. Dubroka, J. Wyzula, A. Slobodeniuk, G. Martinez, Y. Krupko, B. A. Piot, O. Caha, J. Humlíček, G. Bauer, G. Springholz, and M. Orlita, Landau level spectroscopy of Bi_2Te_3, Phys. Rev. B **102**, 085201 (2020).

[9] H. Köhler, Non-parabolic $E(k)$ relation of the lowest conduction band in Bi_2Te_3, Phys. Status Solidi B **73**, 95 (1976).

[10] H. Köhler, Non-parabolicity of the highest valence band of Bi_2Te_3 from Shubnikov–de Haas effect, Phys. Status Solidi B **74**, 591 (1976).

[11] H. Köhler, Anisotropic g-factor of the conduction electrons in Bi_2Te_3, Phys. Status Solidi B **75**, 127 (1976).

[12] H. Schwartz, G. Björck, and O. Beckman, De Haas–van Alphen susceptibility measurements on p-type Sb_2Te_3, Solid State Commun. **5**, 905 (1967).

[13] H. Köhler and A. Freudenberger, Investigation of the highest valence band in $(Bi_{1-x}Sb_x)_2Te_3$ crystals, Phys. Status Solidi B **84**, 195 (1977).

[14] V. A. Kulbachinskii, Z. M. Dashevskii, M. Inoue, M. Sasaki, H. Negishi, W. X. Gao, P. Lostak, J. Horak, and A. de Visser, Valence-band changes in $Sb_{2-x}In_xTe_3$ and $Sb_2Te_{3-y}Se_y$ by transport and Shubnikov–de Haas effect measurements, Phys. Rev. B **52**, 10915 (1995).

[15] W. Zhao, D. Cortie, L. Chen, Z. Li, Z. Yue, and X. Wang, Quantum oscillations in iron-doped single crystals of the topological insulator Sb_2Te_3, Phys. Rev. B **99**, 165133 (2019).

[16] V. Kulbachinskii, D. Zinoviev, V. Kytin, M. Mikhailov, and Z. Ismailov, Thermoelectical properties and Shubnikov–de Haas effect in single crystals $Sb_{2-x}Cu_xTe_3$, Mater. Today: Proc. **44**, 3439 (2021).

[17] A. von Middendorff, K. Dietrich, and G. Landwehr, Shubnikov–de Haas effect in p-type Sb_2Te_3, Solid State Commun. **13**, 443 (1973).

[18] G. Simon and W. Eichler, Investigations on a two-valence band model for Sb_2Te_3, Phys. Status Solidi B **107**, 201 (1981).

[19] G. Wang and T. Cagin, Electronic structure of the thermoelectric materials Bi_2Te_3 and Sb_2Te_3 from first-principles calculations, Phys. Rev. B **76**, 075201 (2007).

[20] B. Y. Yavorsky, N. F. Hinsche, I. Mertig, and P. Zahn, Electronic structure and transport anisotropy of Bi_2Te_3 and Sb_2Te_3, Phys. Rev. B **84**, 165208 (2011).

[21] I. Aguilera, C. Friedrich, G. Bihlmayer, and S. Blügel, *GW* study of topological insulators Bi_2Se_3, Bi_2Te_3, and Sb_2Te_3: Beyond the perturbative one-shot approach, Phys. Rev. B **88**, 045206 (2013).

[22] I. A. Nechaev, I. Aguilera, V. De Renzi, A. di Bona, A. Lodi Rizzini, A. M. Mio, G. Nicotra, A. Politano, S. Scalese, Z. S. Aliev, M. B. Babanly, C. Friedrich, S. Blügel, and E. V. Chulkov, Quasiparticle spectrum and plasmonic excitations in the topological insulator Sb_2Te_3, Phys. Rev. B **91**, 245123 (2015).

[23] I. Aguilera, C. Friedrich, and S. Blügel, Many-body corrected tight-binding Hamiltonians for an accurate quasiparticle description of topological insulators of the Bi_2Se_3 family, Phys. Rev. B **100**, 155147 (2019).

[24] T. L. Anderson and H. B. Krause, Refinement of the Sb_2Te_3 and Sb_2Te_2Se structures and their relationship to nonstoichiometric $Sb_2Te_{3-y}Se_y$ compounds, Acta Crystallogr. Sect. B **30**, 1307 (1974).

[25] A. Dubroka, O. Caha, M. Hronček, P. Friš, M. Orlita, V. Holý, H. Steiner, G. Bauer, G. Springholz, and J. Humlíček, Interband absorption edge in the topological insulators $Bi_2(Te_{1-x}Se_x)_3$, Phys. Rev. B **96**, 235202 (2017).

[26] www.flapw.de.

[27] C. Friedrich, S. Blügel, and A. Schindlmayr, Efficient implementation of the *GW* approximation within the all-electron FLAPW method, Phys. Rev. B **81**, 125102 (2010).

[28] J. P. Perdew, K. Burke, and M. Ernzerhof, Generalized gradient approximation made simple, Phys. Rev. Lett. **77**, 3865 (1996).

[29] I. Aguilera, C. Friedrich, and S. Blügel, Spin-orbit coupling in quasiparticle studies of topological insulators, Phys. Rev. B **88**, 165136 (2013).

[30] R. Sakuma, C. Friedrich, T. Miyake, S. Blügel, and F. Aryasetiawan, *GW* calculations including spin-orbit coupling: Application to Hg chalcogenides, Phys. Rev. B **84**, 085144 (2011).

[31] N. Marzari, A. A. Mostofi, J. R. Yates, I. Souza, and D. Vanderbilt, Maximally localized Wannier functions: Theory and applications, Rev. Mod. Phys. **84**, 1419 (2012).

[32] A. A. Mostofi, J. R. Yates, Y.-S. Lee, I. Souza, D. Vanderbilt, and N. Marzari, Wannier90: A tool for obtaining maximally-localised Wannier functions, Comput. Phys. Commun. **178**, 685 (2008).

[33] S. Zhu, Y. Ishida, K. Kuroda, K. Sumida, M. Ye, J. Wang, H. Pan, M. Taniguchi, S. Qiao, S. Shin, and A. Kimura, Ultrafast electron dynamics at the Dirac node of the topological insulator Sb_2Te_3, Sci. Rep. **5**, 13213 (2015).

[34] H. E. Lund, K. Volckaert, P. Majchrzak, A. J. H. Jones, M. Bianchi, M. Bremholm, and P. Hofmann, Bulk band structure of Sb_2Te_3 determined by angle-resolved photoemission spectroscopy, Phys. Chem. Chem. Phys. **23**, 26401 (2021).

[35] L. Locatelli, A. Kumar, P. Tsipas, A. Dimoulas, E. Longo, and R. Mantovan, Magnetotransport and ARPES studies of the topological insulators Sb_2Te_3 and Bi_2Te_3 grown by MOCVD on large-area Si substrates, Sci. Rep. **12**, 3891 (2022).

[36] O. Ly and D. M. Basko, Theory of electron spin resonance in bulk topological insulators Bi_2Se_3, Bi_2Te_3 and Sb_2Te_3, J. Phys.: Condens. Matter **28**, 155801 (2016).

[37] C.-X. Liu, X.-L. Qi, H. J. Zhang, X. Dai, Z. Fang, and S.-C. Zhang, Model Hamiltonian for topological insulators, Phys. Rev. B **82**, 045122 (2010).

[38] B. A. Assaf, T. Phuphachong, V. V. Volobuev, A. Inhofer, G. Bauer, G. Springholz, L. A. de Vaulchier, and Y. Guldner, Massive and massless Dirac fermions in $Pb_{1-x}Sn_xTe$ topological crystalline insulator probed by magneto-optical absorption, Sci. Rep. **6**, 20323 (2016).

[39] K. K. Tikuišis, J. Wyzula, L. Ohnoutek, P. Cejpek, K. Uhlířová, M. Hakl, C. Faugeras, K. Výborný, A. Ishida, M. Veis, and M. Orlita, Landau level spectroscopy of the PbSnSe topological crystalline insulator, Phys. Rev. B **103**, 155304 (2021).

[40] E. Burstein, Anomalous optical absorption limit in InSb, Phys. Rev. **93**, 632 (1954).

[41] T. S. Moss, The interpretation of the properties of indium antimonide, Proc. Phys. Soc. B **67**, 775 (1954).

[42] V. Bragaglia, M. Ramsteiner, D. Schick, J. E. Boschker, R. Mitzner, R. Calarco, and K. Holldack, Phonon anharmonicities and ultrafast dynamics in epitaxial Sb_2Te_3, Sci. Rep. **10**, 12962 (2020).

[43] R. J. Cava, H. Ji, M. K. Fuccillo, Q. D. Gibson, and Y. S. Hor, Crystal structure and chemistry of topological insulators, J. Mater. Chem. C **1**, 3176 (2013).

[44] J. Horak, C. Drasar, R. Novotny, S. Karamazov, and P. Lostak, Non-stoichiometry of the crystal lattice of antimony telluride, Phys. Status Solidi A **149**, 549 (1995).

[45] I. Rajput, D. Kumar, and A. Lakhani, Empirical role of crystalline defects in the transport properties of Sb_2Te_3 single crystals, Cryst. Growth Des. **23**, 6019 (2023).

[46] H. Köhler and E. Wöchner, The *g*-factor of the conduction electrons in Bi_2Se_3, Phys. Status Solidi B **67**, 665 (1975).

[47] C. Weyrich, T. Merzenich, J. Kampmeier, I. E. Batov, G. Mussler, J. Schubert, D. Grützmacher, and T. Schäpers, Magnetoresistance oscillations in MBE-grown Sb_2Te_3 thin films, Appl. Phys. Lett. **110**, 092104 (2017).

[48] P. Y. Yu and M. Cardona, *Fundamentals of Semiconductors: Physics and Materials Properties* (Springer, Berlin, Heidelberg, 1996).

[49] M. Eschbach, E. Młyńczak, J. Kellner, J. Kampmeier, M. Lanius, E. Neumann, C. Weyrich, M. Gehlmann, P. Gospodarič, S. Döring, G. Mussler, N. Demarina, M. Luysberg, G. Bihlmayer, T. Schäpers, L. Plucinski, S. Blügel, M. Morgenstern, C. M. Schneider, and D. Grützmacher, Realization of a vertical topological p–n junction in epitaxial Sb_2Te_3/Bi_2Te_3 heterostructures, Nat. Commun. **6**, 8816 (2015).